Tensile Lattice Distortion Does Not Affect Oxygen Transport in Yttria-Stabilized Zirconia–CeO_2 Heterointerfaces

Daniele Pergolesi,[†] Emiliana Fabbri,[†] Stuart N. Cook,[‡] Vladimir Roddatis,[§] Enrico Traversa,[⊥,*] and John A. Kilner[‡,§,*]

[†]International Center for Materials Nanoarchitectonics (WPI-MANA), National Institute for Materials Science (NIMS), 1-1 Namiki, Tsukuba, Ibaraki 305-0044 Japan, [‡]Department of Materials, Imperial College London, London SW7 2BP, United Kingdom, [§]CIC Energigune, Albert Einstein 48, 01510 Miñano (Álava), Spain, and [⊥]International Research Center for Renewable Energy, State Key Laboratory of Multiphase Flow in Power Engineering, Xi'an Jiaotong University, Xi'an, Shaanxi 710049, China

ABSTRACT Biaxially textured epitaxial thin-film heterostructures of ceria and 8 mol % yttria-stabilized zirconia (8YSZ) were grown using pulsed laser deposition (PLD) with the aim to unravel the effect of the interfacial conductivity on the charge transport properties. Five different samples were fabricated, keeping the total thickness constant (300 nm), but with a different number of heterointerfaces (between 4 and 60). To remove any potential contribution of the deposition substrate to the total conductivity, the heterostructures were grown on (001)-oriented MgO single-crystalline wafers. Layers free of high-angle grain boundaries and with low density of misfit dislocations were obtained, as revealed by X-ray diffraction (XRD) and high-resolution transmission electron microscopy (HR-TEM) analysis. The crystallographic quality of these samples allowed the investigation of their conduction properties, suppressing any transport effects along grain boundaries and/or interfacial dislocation pathways. Electrochemical impedance spectroscopy (EIS) and secondary ion mass spectroscopy (SIMS) measurements showed that for these samples the interfacial conductivity has a negligible effect on the transport properties.

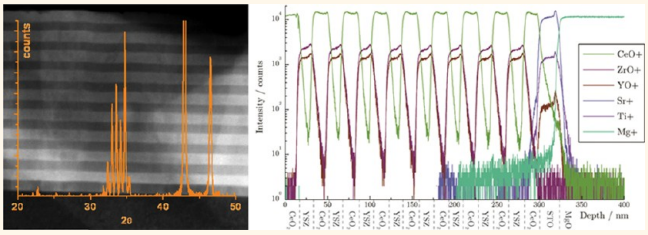

KEYWORDS: pulsed laser deposition · superlattice · heterostructure · interface · strain · oxygen-ion conducting oxides · secondary ion mass spectrometry

Recent experimental evidence has shown that interfacial phenomena at thin-film heterophase interfaces of oxygen-ion conducting oxides can significantly deviate from those of the oxide bulk, giving rise to faster or slower ion conduction pathways, depending on the structural mismatch at the interface.[1−3] Such interfacial phenomena are often generally ascribed to strain effects.[4−9]

A strained interface is the consequence of the structural mismatch between the two constituent materials (film on substrate or multilayers). An elastically strained and coherent interface between two materials can be fabricated when the two adjacent layers have relatively small difference in lattice parameter and symmetry and when the two materials show an almost ideal layer-by-layer growth mechanism, allowing the formation of atomically smooth interfaces. When the structural mismatch between the two materials becomes too large to be elastically accommodated, the strain is released and relaxation occurs *via* the introduction of lattice defects and/or misfit dislocations (*i.e.*, extra lattice planes are introduced on the side of the material with the smaller lattice parameter). Finally, further increasing the lattice mismatch inevitably leads to a complete breaking of the crystalline symmetry with the formation of disordered or "incoherent" interfaces.[10]

The excess strain can also relax through the formation of irregularities at the interface, such as, for example, a pronounced interfacial roughness, and by breaking the crystalline symmetry introducing grain boundaries. In particular, for the case of polycrystalline thin films (or epitaxial thin films with

* Address correspondence to j.kilner@imperial.ac.uk, traversa.enrico@gmail.com.

Received for review June 25, 2012 and accepted October 29, 2012.

Published online October 29, 2012
10.1021/nn302812m

columnar morphology), the effective average strain field is difficult to evaluate, and the alternative conduction pathway along and across grain boundaries can hinder the identification of the effect of the interfacial conductivity.

Only in the ideal case of samples free from grain boundaries, with "coherent" and atomically flat interfaces, can the lattice strain be directly correlated with the lattice mismatch between the adjacent layers and hence the potential effect of an interfacial conduction pathway arising from the strain be easily identified (considering in-plane measurements).

To the best of our knowledge, the only literature reports on the fabrication of grain-boundary-free heterostructures comprising an oxygen-ion conductor and an insulating phase, showing coherent, highly strained, and atomically flat interfaces are those for (100) $SrTiO_3$ (STO) substrates.[6,9] However, STO is not a good insulator at high temperatures, and conductivity measurements of thin films deposited on STO might be significantly affected by the substrate.[11]

The (100) and (110) MgO substrates, for which the insulating properties at high temperatures are well-demonstrated, have been used for the fabrication of grain-boundary-free ultrathin 8.7 mol % yttria-stabilized zirconia (8.7YSZ; note, in this paper, yttria concentrations in yttria-stabilized zirconia will be quoted as *n*YSZ, where *n* is the concentration in mol %) layers.[9] An increase in conductivity of 3.5 orders of magnitude was measured and ascribed to interfacial effects. However, the lattice misfit between 8.7YSZ and MgO, as large as −18%, was primarily released by misfit dislocations, and the large increase in conductivity was attributed to conduction pathways along dislocation lines.

The use of insulating substrates such as MgO or Al_2O_3 for the growth of heterostructures made of an oxygen-ion conducting oxide and an insulating phase often led to polycrystalline microstructures, and several conductivity measurements have been reported using polycrystalline films, often with columnar morphology.[7,10,12−16] Polycrystalline 9.5YSZ-Y_2O_3 multilayered films $\{(0001)\ Al_2O_3|Y_2O_3|\ (9.5YSZ|Y_2O_3) \times n\}$ grown on sapphire substrates with (quasi-)coherent heterointerfaces along each columnar grain showed that the conductivity slightly increased and the activation energy slightly decreased with increasing the number of interfaces.[10] According to the authors, the grain boundary conduction pathway played a negligible role in the charge transport. However, the conductivity of every sample was smaller than the conductivity of YSZ polycrystalline films with comparable average grain size (samples with 40 interfaces at 560 °C showed conductivity 4-fold smaller than the conductivity of YSZ polycrystalline films[17]).

In general, literature data are quite consistent concerning the increased oxygen-ion conductivity of interfaces showing a large dislocation density,[4,7,9] but whether the interfacial strain can play a significant role in enhancing the ionic conductivity is still quite a controversial issue.

TABLE 1. Design of the Five Heterostructures Fabricated and Tested

sample	number of bilayers	bilayer thickness (nm)	number of interfaces
A	2	120	4
B	4	70	8
C	8	35	16
D	16	18	32
E	30	10	60

In this work, we present the fabrication and characterization of multilayered heterostructures made of an oxygen-ion conducting oxide, 8YSZ, and a more insulating phase, CeO_2. Comparing the electrical conductivities of the two materials, the total ionic conductivity of the epitaxial CeO_2 films is on the order of 10^{-3} S/cm at 700 °C,[18] while 8YSZ shows a bulk conductivity more than 1 order of magnitude larger at the same temperature.[19] The 8YSZ-CeO_2 heterostructures were grown biaxially textured on insulating (001) MgO substrates and showed a very small density of interfacial dislocations. In such samples, only the residual interfacial strain is expected to be potentially able to add a further parallel contribution to the total conductivity. To unravel a possible enhancement in conductivity at the interfaces between 8YSZ and CeO_2, we varied the number of interfaces (from 4 up to 60) keeping constant the total thickness of the heterostructures (300 nm).

The heterostructures were fabricated by pulsed laser deposition (PLD) stacking up several layers of 8YSZ and CeO_2 on (001) MgO wafers. A 10 nm thick seed layer of $SrTiO_3$ (STO), epitaxially oriented with the (001) MgO substrate, allowed the heterostructures to grow with high crystallographic quality without introducing any significant contribution to the conducting properties of the samples.

RESULTS AND DISCUSSION

Structural, Morphological, and Chemical Characterization. Five biaxially textured sets of 8YSZ-CeO_2 heterostructures were fabricated on (001) MgO single-crystalline substrates keeping the total thickness approximately constant (300 nm) and varying the number of the YSZ-CeO_2 bilayers, according to the scheme

$$MgO - STO - CeO_2 - (8YSZ + CeO_2) \times n$$

where *n* is the number of 8YSZ-CeO_2 bilayers, equal to 2, 4, 8, 16, and 30, while the thickness of each individual bilayer was about 120, 70, 35, 18, and 10 nm, respectively. Table 1 summarizes the characteristics of the samples that are labeled as sample A, B, C, D, and E. Since each heterostructure starts and ends with an insulating CeO_2 layer, the selected design ensures a

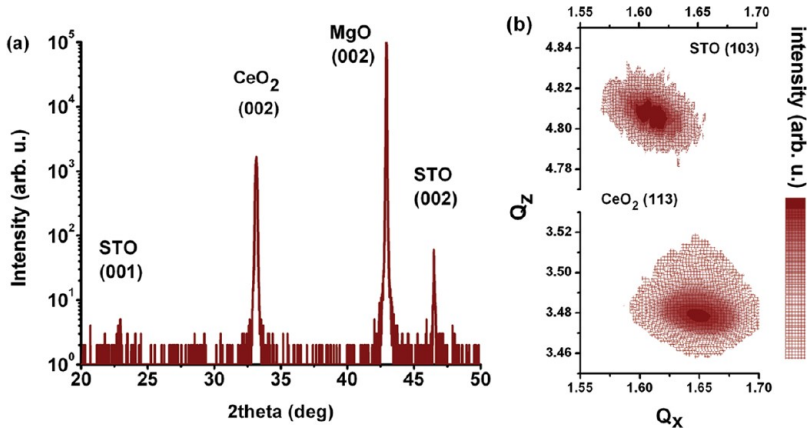

Figure 1. (a) A $2\theta-\theta$ scan and (b) reciprocal space maps (RSM) of a CeO_2 film grown (001) epitaxial oriented and biaxially textured on a (001) MgO substrate by means of a thin epitaxial buffer layer of STO.

symmetric arrangement for the ionically conducting 8YSZ layers.

The highly textured growth of the [(8YSZ+CeO_2) × *n*] heterostructures strongly depends on the crystalline quality of the MgO-STO-CeO_2 structures, which provide the required crystalline template. MgO, STO, and CeO_2 have the same cubic symmetry but different crystalline structures (rock salt, perovskite, and fluorite, respectively) and different lattice parameters (about 4.21, 3.90, and 5.41 Å, respectively).

STO-CeO_2 bilayers can grow epitaxially oriented and biaxially textured on MgO substrates according with the epitaxial relation [001] MgO//[001] STO//[001] CeO_2 and [100] MgO//[100] STO//[110] CeO_2.[20] The growth of such template structures was analyzed in detail by X-ray diffraction (XRD) analysis using 300 nm thick CeO_2 films grown on an 80 nm thick STO buffer layer deposited *in situ* on a (001) MgO substrate. Figure 1a shows the $2\theta/\theta$ scan that revealed the epitaxial orientation of the STO-CeO_2 bilayer with the MgO substrate. The same figure also reports the measurements of the reciprocal space maps in terms of in-plane (Qx) and out-of-plane (Qz) reciprocal vectors (Figure 1b) acquired toward the asymmetric reflections (103) and (113) for STO and CeO_2, respectively. Phi scans were also performed along the same asymmetric reflections and showed the same results reported in ref 20. These measurements, together with the high-resolution scanning transmission electron microscopy (HR-STEM) analysis reported here below, showed the biaxial texture of the STO-CeO_2 bilayer.

Within the limits of the technique, the evaluation of the lattice parameters for these relatively thick layers showed an almost fully relaxed crystalline structure for both layers (Figure 1b), as expected for such relatively large thicknesses.

The very similar value of Qx found for STO and CeO_2 toward two asymmetric reflections mutually rotated in-plane by 45° is a further confirmation of the in-plane symmetry of the STO-CeO_2 bilayer.

The deposition of the [(8YSZ+CeO_2) × *n*] heterostructures was performed *in situ* onto the surface of the MgO-STO-CeO_2 template structures described above.

As internal reference for the electrical characterization, thin films of 8YSZ about 150 nm thick were also grown by PLD on (001)-oriented MgO wafers. In spite of the large lattice mismatch between YSZ (5.14 Å) and MgO (4.21 Å), epitaxial films were obtained, as revealed by XRD analysis, with a relatively broad (002) rocking curve (ω scan), with a fwhm of approximately 0.64°.

Figure 2 shows the $2\theta-\theta$ scan of the five 8YSZ-CeO_2 heterostructures. Every sample showed epitaxial orientation with the deposition substrate. For the A (Figure 2a), B (Figure 2b), and C (Figure 2c) samples, the (002) reflection lines of the two materials CeO_2 (at $2\theta \approx 33°$) and 8YSZ (at $2\theta \approx 35°$) could be clearly identified, even though for sample C the superlattice modulation started overlapping with the two reflection lines. In the case of the sample D (Figure 2d), the superlattice modulation completely overlapped the reflection lines of the two materials. Finally, sample E (Figure 2e) showed the typical feature of a superlattice with an average structure peak surrounded by clearly identifiable first- and second-order satellite peaks. Sharp and well-defined satellite peaks suggest a very high quality of the interfaces between the two constituent oxides. The relative angular position of the satellite peaks allows a calculation of the thickness Λ of each individual bilayer according to the equation: $\Lambda = \lambda/(\sin\theta_{+1} - \sin\theta_{-1})$, where θ_{+1} and θ_{-1} are the angular positions of the two first-order satellite peaks and λ is the X-ray wavelength (Cu Kα, $\lambda \approx 1.540$ Å). For the sample E, this calculation gave $\Lambda = 97.5$ Å, in very good agreement with the expected thickness (about 100 Å), as derived from the calibration of the deposition rate performed by X-ray reflectometry (XRR). Figure 2f shows the XRR measurements performed on epitaxially oriented thin films of CeO_2 and 8YSZ deposited on (001)-oriented STO and MgO substrates, respectively. A deposition rate of about 0.45 Å/shot was measured for CeO_2, while

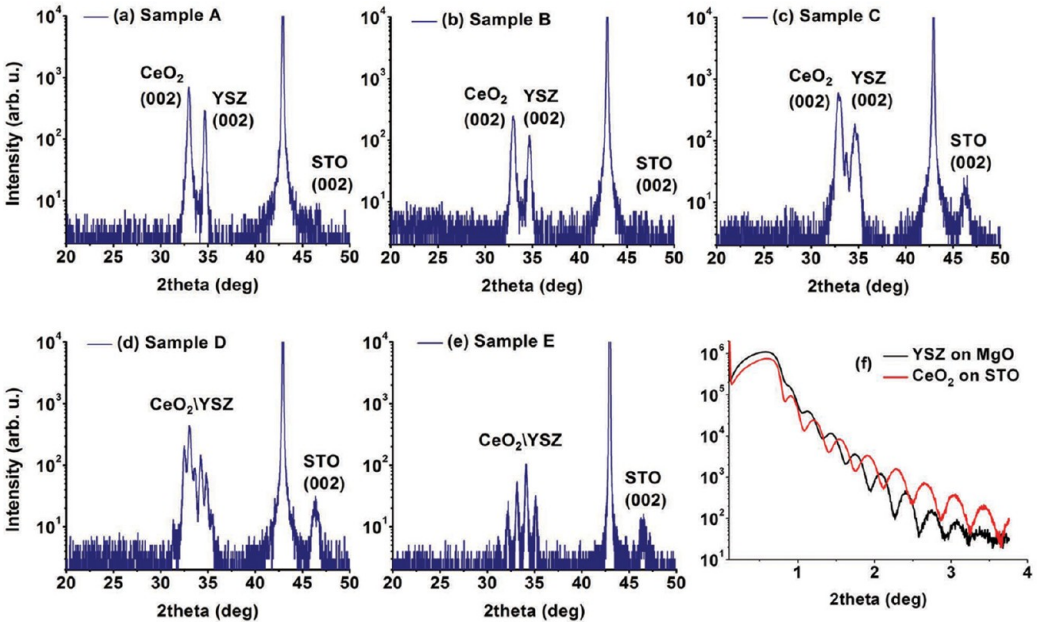

Figure 2. X-ray diffraction (XRD) plots of the five heterostructures from (a) to (e) fabricated for this work. (f) X-ray reflectometry (XRR) measurements of the deposition rates of CeO_2 and 8YSZ.

a value roughly 4-fold smaller was found for 8YSZ (about 0.13 Å/shot). These measurements allowed the deposition of symmetric bilayers, that is, almost equal thickness for the two materials for each bilayer, by selecting the appropriate number of laser shots on each target.

HR-STEM analysis was used for the local microstructural characterization of the samples. Figure 3a shows a typical high-angle annular dark-field image of a heterostructure (sample E), acquired in the [110] direction of CeO_2 (or 8YSZ), while a HR-STEM micrograph is shown in Figure 3b. Continuous and well-defined bilayers of the two materials, as well as the STO seed layer, are clearly visible. The analysis of selected area electron diffraction (SAED) patterns acquired in different regions along the cross section revealed that each layer consisted of epitaxial mosaic domains having various crystallographic tilts within a range of about $\pm 2.5°$ with respect to the direction normal to the substrate. This epitaxial misorientation was mainly observed for the 8YSZ layers[21] and was much larger than that measured in the case of single films of CeO_2 or 8YSZ that showed a value of the fwhm of the ω scan of about 0.3−0.5°. Several types of defects in the heteroepitaxial films (*i.e.*, angular rotation, local strain, lattice bending) can result in divergent angles of the crystallographic orientations.[21] In the case of heterostructures made of several thin layers (62 in the case of sample E), the cumulative effect of such small tilts around the growth direction could give rise to the observed overall precession of the growth direction. Moreover, the different thermal expansion coefficients of the four materials used for the fabrication of the heterostructures could justify the geometrical bending

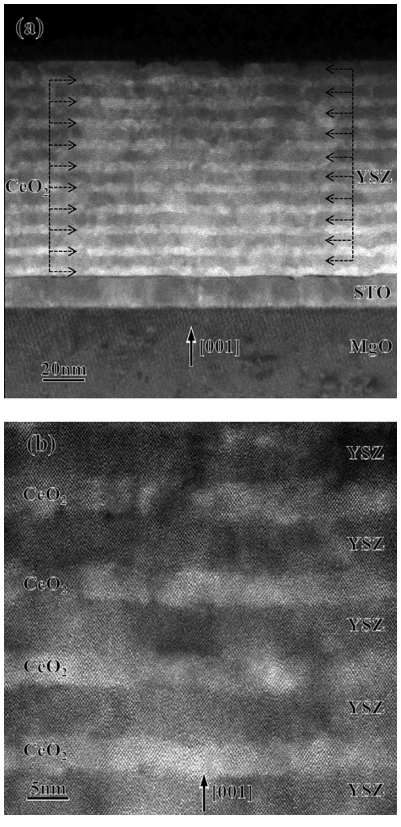

Figure 3. Cross section high-angle annular dark-field micrograph along the [110] direction (a) and high-resolution scanning transmission electron microscopy (HR-STEM) micrograph (b) of sample E.

of the lattice planes with a consequent enhancement of the mosaic dispersion when the sample is cooled from the deposition temperature (700 °C) to room temperature.

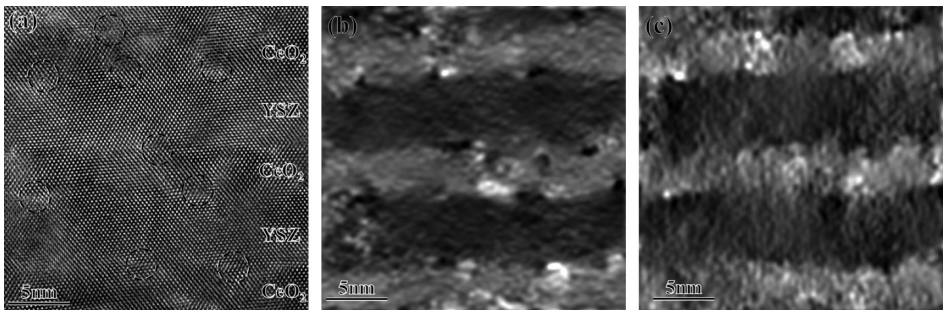

Figure 4. Bright-field HRTEM image of sample E (a) and corresponding maps of the distribution of the strains ε_{xx} (b) and ε_{yy} (c). Some dislocations are marked with circles on (a).

An average thickness of about 4.5 and 6 nm was measured for the CeO_2 and the YSZ layers, respectively (Figure 3b), in good agreement with the expected value of 5 nm. The interfaces showed an average roughness of about 1 nm. In agreement with the XRD analysis, no evidence of misoriented grains was observed, with the exception of few and isolated small grains in the region close to the STO buffer layer, as shown in Figure S1a,b in the Supporting Information.

Theoretical simulations based on amorphization and recrystallization of CeO_2-6.7YSZ multilayered structures[22] showed that during the crystallization the system passes through a polycrystalline microstructure that evolves toward a single-crystalline matrix interrupted by misoriented grains. Since the polycrystalline structure is of higher energy than the single crystal, such misoriented grains reduce their size with time toward a complete annealing and a full dissolution. Our experimental HR-TEM images show a marked resemblance to the sphere model representation of the theoretical simulation reported in ref 22, and indeed, we observed the presence of such misoriented grains that were not annealed out during the film growth. Interestingly, all of these grains showed epitaxial out-of-plane orientation and a 45° rotation in-plane. Only a few isolated defects induced by the local inhomogeneity of the STO seed layer were observed (see Supporting Information Figure S2).

Geometric phase analysis (GPA) was used to confirm the presence of strains along the layers. Omitting the mathematical basis of the GPA method,[23] and the basic equations of the algorithm of digital processing of HR-TEM images,[24] here only a brief phenomenological description is presented. The stress in a HR-TEM image is reflected by the presence of variations in the lattice periods. Each periodicity in a HR-TEM image is represented by a spot in the corresponding Fourier transformation. By analyzing the intensity distribution around the spot in the Fourier transform, it is possible to directly determine the distribution of variations in the corresponding interplanar spacing in a HR-TEM image. Usually, the result of GPA analysis is presented by a color map where each point corresponds to a local value of the interplanar spacing. In the case of the presence of two unstrained ideal materials with different lattice parameters, just parallel strips of different uniform colors (corresponding to the different materials) would be visible.

Considering the lattice parameters of CeO_2 ($c = 5.41$ Å) and 8YSZ ($c = 5.14$ Å), 8YSZ shows a lattice misfit of about 5.1% with respect to CeO_2. Digital processing of the experimental HR-TEM images was performed by the GPA method using the same approach as described in ref 24. HR-TEM micrographs of sample E and corresponding maps of the distribution of the strains ε_{xx} and ε_{yy} are shown in Figure 4. According to these maps, the 8YSZ and CeO_2 layers are significantly but non-uniformly distorted in both directions within the range from 0 up to 5% (the lattice misfit of the bulk materials).

Similar results were obtained by analyzing the reciprocal space maps acquired for CeO_2-8YSZ superlattices (Figure S3).

The introduction of misfit dislocations in thin-film structures has been recognized to be the primary mechanism for accommodating the lattice mismatch between CeO_2 and 8YSZ[21] and CeO_2 and 7YSZ.[25] Theoretical simulation of the crystalline evolution of a 6.7YSZ-CeO_2 multilayer[22] foresees the presence of a regular array of misfit dislocations at the interface to release the strain. Owing to the larger lattice constant of CeO_2 than that of 6.7YSZ, extra planes of misfit dislocations on the YSZ side are expected to appear with an average spacing of about 7 nm, with a consequent drastic reduction of the lattice misfit from 5.1 down to 0.7%. A regular array of such a dislocation network with an average spacing of about 3.9 nm was experimentally observed in CeO_2-8YSZ bilayers deposited by PLD on Si.[21] An average spacing between dislocations of about 3.3 nm was observed in the case of epitaxial films of CeO_2 grown by molecular beam epitaxy on (001)-oriented 7YSZ single crystals.[25] The analysis of several HR-TEM micrographs acquired for sample E showed an average total dislocation density of about 3×10^{12} cm^{-2}. A very similar value of dislocation density, or even lower, was found for heterostructures fabricated by coupling 9.5YSZ with Y, Lu, and Sc oxides,[13] and the interfaces were described as (quasi-)coherent.

For sample E, most of the identified dislocations quite clearly accounted for interface dislocations and appeared more randomly distributed rather than organized in a sort of regular network. The calculated average spacing

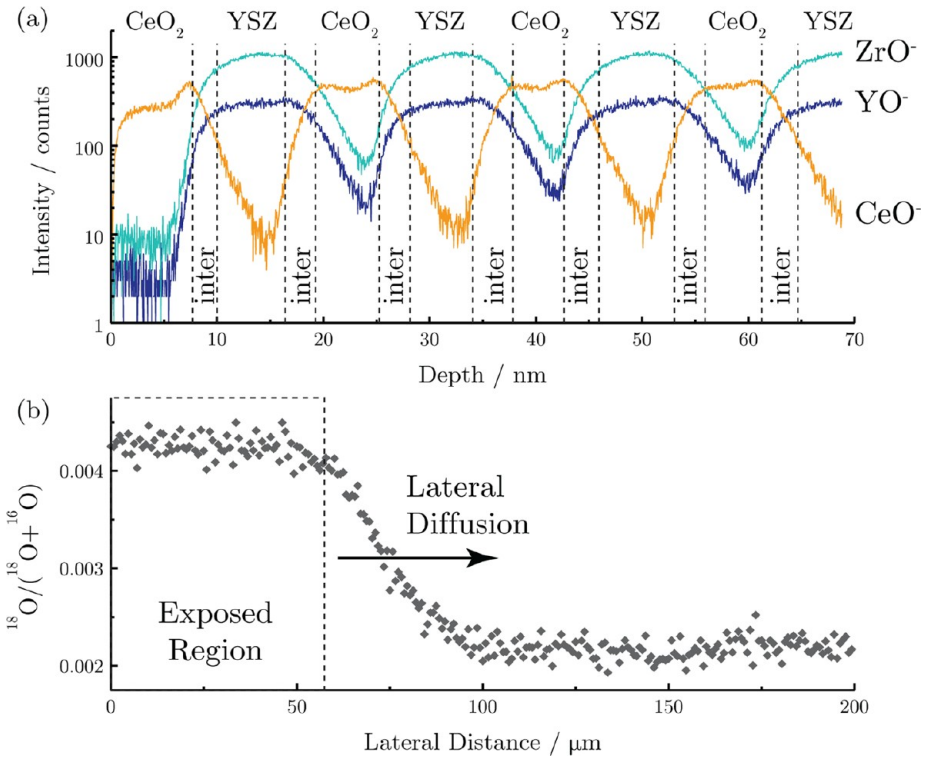

Figure 5. (a) Depth profile through the top 70 nm of sample D with demarcations indicating the layer classification and (b) lateral isotopic profile from the masked and subsequently exposed region on the left and the measured diffusion profile, indicated.

between adjacent interfacial dislocations was between 6 and 7 nm. This value is very similar to that predicted by theoretical simulation[22] and is almost twice the value reported in the literature for similar heterostructures.[21,25]

The interfacial roughness observed in our samples is probably the reason that prevented the self-organization of the dislocations at the interfaces into a more regular array and that justifies the non-uniform strain field, as revealed by GPA analysis. The reflection high energy electron diffraction (RHEED) patterns acquired during the growth of the CeO_2 layers[26] showed the typical features of a three-dimensional growth mechanism, which could be responsible for the enhanced interface roughness. Due to the interfacial roughness, the continuity of adjacent lattice planes across the interfaces could not be unambiguously tracked over large areas, thus precluding a reliable estimation of the strength of the residual strain field.

Time-of-flight secondary mass spectroscopy (ToF-SIMS) was utilized to investigate the depth-dependent composition of samples A–D and revealed sharp interfaces over extended (100 × 100 μm) areas together with minimal contamination in the layers. The analysis of sample C is shown in Figure S4 in the Supporting Information as an example. Further details are given in the Supporting Information.

Lateral Oxygen Diffusion Measurements. Oxygen tracer diffusion measurements were performed on sample D (featuring 16 bilayers, each of 18 nm thickness) in order to investigate the extent of diffusion in the layers along a lateral direction.

Figure 5 shows a compositional depth profile obtained from the 3-D SIMS data set by summing the $x-y$ analysis planes. This depth profile was then used to separate the data set into three types of layers along the z axis: YSZ, CeO_2, or an "interlayer". This interlayer is defined as a region where the lack of depth resolution and the crater roughness make the composition difficult to categorize. The individual layer types are annotated on the depth profile in Figure 5a, indicating the scheme used. Once these categories were determined, the data could be separated into layers and that for each layer of the same type summed, for each ion species, along the z axis, producing three separate $X-Y$ ion image sets. Of central interest is the distribution of oxygen isotope within the 8YSZ and CeO_2 layers in the x direction away from the exposed region. To obtain good statistics, ion images of the $^{16}O^-$ and $^{18}O^-$ species were summed along rows parallel to the gold edge (on the y axis) in order to produce line scans in the x direction. The ^{18}O fraction (c^*) was then calculated from the line scans as follows:

$$c^* = \frac{[^{18}O]}{[^{18}O] + [^{16}O]}$$

An example of a line scan obtained in such a manner is shown in Figure 5b.

In the region of sample exposed to the ^{18}O-enriched atmosphere, there was very little variation in c^* with

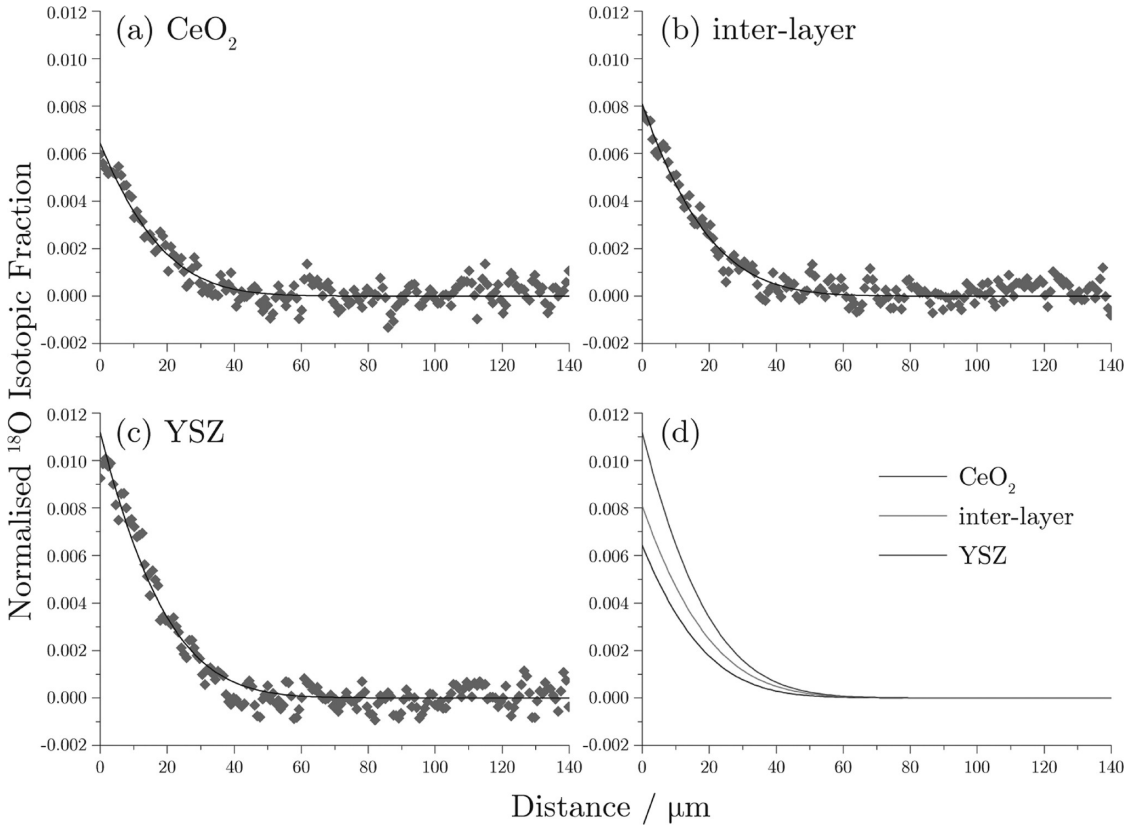

Figure 6. Isotopic fraction against depth for the CeO_2 (a), interlayer (b), and YSZ layer types (c) with the combined fitted diffusion profiles (d) for an exchange performed at 487 °C, anneal time ~3280 s, pO_2 = 200 mbar.

depth, throughout the films. In order to obtain values of D^* (tracer diffusion coefficient) and k^* (tracer exchange coefficient), the normalized ^{18}O concentration profile from the gold edge ($c_r^*(x)$ against x) is fitted to the solution of Fick's second law for diffusion in a semi-infinite medium with surface limitation as given by Crank:[27]

$$c_r^* = \frac{c^*(x) - c_{bg}^*}{c_g^* - c_{bg}^*} = \mathrm{erfc}\left(\frac{x}{2\sqrt{D^* t}}\right) - \exp\left(\frac{k^* x}{D^*} + \frac{k^{*2} t}{D^*}\right) \times \mathrm{erfc}\left(\frac{x}{2\sqrt{D^* t}} + k^* \sqrt{\frac{t}{D^*}}\right)$$

where c_{bg}^* is the background ^{18}O concentration (measured at 0.0022) and c_g^* is the ^{18}O concentration of the annealing gas (0.258). The profiles obtained for each layer type were fitted to this equation using a regression analysis fit in Matlab.[28] Results from these fittings are detailed in Table 2 as well as their goodness of fit (χ^2); the data and fitted profiles are shown in Figure 6.

The inherent inaccuracy of edge determination and the fact that the true surface is not well-defined will lead to a great deal of error in the surface exchange coefficient (k^*) values with these measurements; however, of primary interest is the diffusivity (D^*) values. All three layer types, CeO_2, 8YSZ, and interlayer, show D^* values which are very similar in magnitude. This effect

TABLE 2. Tracer Diffusion Coefficient (D^*) and Tracer Exchange Coefficient (k^*) Values for Each Layer Type

layer	D^*/cm^2 s^{-1}	k^*/cm s^{-1}	χ^2
CeO_2	8.37×10^{-10}	2.89×10^{-9}	0.002
interlayer	9.68×10^{-10}	3.91×10^{-9}	0.016
YSZ	9.57×10^{-10}	5.39×10^{-9}	0.015

was expected and is due to the aspect ratio of the structures. While the measurements are made on the scale of tens of micrometers in the lateral direction, diffusion between films, once the ^{18}O is some distance from the edge, is only a matter of a few nanometers, hence oxygen transfer between layers is facile. This effect has previously been discussed by Perkins *et al.* in multilayers of alternating samarium-doped ceria and undoped ceria.[29]

Using the Nernst–Einstein equation,[30] it is possible to relate the oxygen-ion diffusion coefficient and its conductivity contribution. The values at 478 °C were calculated for the YSZ layer at 5.4×10^{-5} S cm^{-1} and for the CeO_2 layer at 4.2×10^{-5} S cm^{-1}. The value in the undoped ceria layers will, in this case, be enhanced due to the interdiffusion of tracer between layers, discussed previously. If the conductivity in the 8YSZ layers is considered, however, this value is seen to be in good agreement with that measured by EIS (about 1.3×10^{-5} S cm^{-1}), reported later (Figure 8), confirming that the

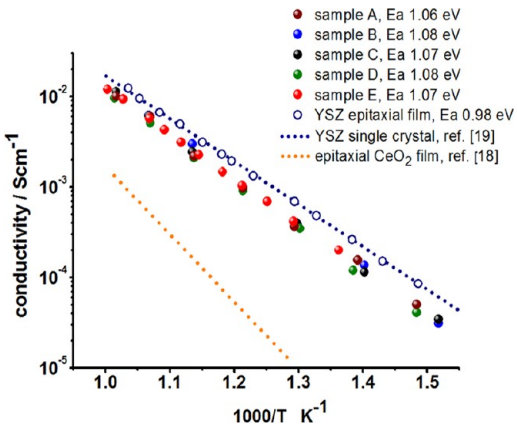

Figure 7. Arrhenius plots measured for samples A–E and for a highly textured 8YSZ film. For reference, the conductivities of bulk 9.5YSZ and of epitaxial CeO_2 film are also reported.

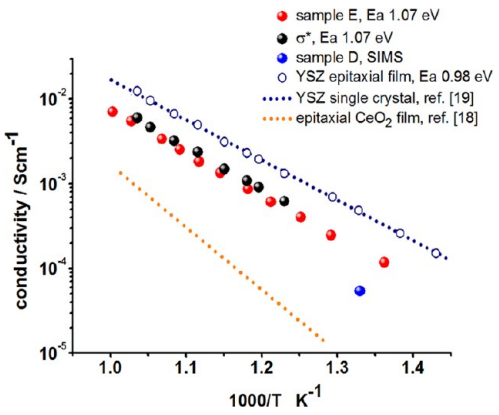

Figure 8. Comparison between the conductivity of sample E and the conductivity of a hypothetical highly textured and fully relaxed bilayer of CeO_2 and 8YSZ. The conductivity of sample D calculated using the diffusion coefficient measured by SIMS is also reported.

dominant charge carrier is indeed oxygen. The conductivity values derived by EIS and SIMS at about 480 °C differ by only about a factor of 2, which is an acceptable difference, given the very different nature of the two measuring techniques.

Electrical Characterization. In-plane EIS measurements were performed in air between 400 and 700 °C. The MgO substrate with a 10 nm thick STO buffer layer was initially characterized. The resulting conductivity of the STO layer was about 10^{-4} S cm^{-1} at 700 °C. At the same temperature, CeO_2 epitaxial films showed a conductivity more than 1 order of magnitude larger,[18] in turn more than 2 orders of magnitude smaller than the bulk conductivity of 9.5YSZ.[19]

As discussed previously, thin oxide films grown by PLD at high temperature and in relatively low oxygen partial pressure are typically partially reduced. During the electrical characterization, performed in air up to a maximum temperature of 700 °C, the heterostructures undergo an oxidizing anneal. To check the microstructural stability of the samples, $2\theta-\theta$ scans were measured after the film growth and after the electrical characterization without observing any significant difference.

Figure 7 shows the Arrhenius plots measured for all of the multilayers, as well as for the 8YSZ thin film grown epitaxially oriented on MgO, used as an internal reference for this work. The same plot also reports literature data of the conductivity of 9.5YSZ single crystal,[19] as well as of the conductivity of epitaxially oriented CeO_2 films grown by PLD.[18] To evaluate the resistivity of the different heterostructures at each temperature, only the sum of the thicknesses of the 8YSZ layers was taken into account.

As a first observation, the conductivity and the activation energy of the highly textured 8YSZ film matched very well the conductivity of 9.5YSZ single crystal, meaning that the ablation process used for this work resulted in 8YSZ films with the expected conducting properties.

A second important finding was that the five heterostructures showed basically the same values of conductivity and activation energy (between 1.06 and 1.10 eV), without any significant trend proportional to the increasing number of interfaces from 4 (sample A) to 60 (sample E). Slightly smaller conductivities than 8YSZ bulk were measured at high temperatures, while the small difference in activation energy resulted in a more pronounced divergence at low temperatures (about a factor of 2 at 500 °C).

The experimental results obtained in this work can be easily explained on the basis of the following analysis. Let us compare the conductivity of our heterostructures with the conductivity of a hypothetical sample consisting on a bilayer of CeO_2 and 8YSZ with conductivities σ_{CeO_2} and σ_{YSZ}, where σ_{CeO_2} and σ_{YSZ} are the conductivities of highly textured and fully relaxed films of CeO_2[17] and of 8YSZ (this work, or equivalently ref 18).

In our heterostructures, the 8YSZ volume content varies from a minimum of 40% for sample A up to a maximum of almost 50% for sample E. Selecting sample E as an example, we can design this hypothetical bilayer in symmetric configuration with the two layers of the same thickness. Finally, assuming the two materials acting in parallel independently of one another, the conductivity of such a bilayer can be written as $\sigma^* = 1/2\ (\sigma_{CeO_2} + \sigma_{YSZ})$.

Figure 8 shows the comparison between σ^*, calculated as described above, and the conductivity measured for sample E, calculated considering the whole thickness of the deposition (about 300 nm). Figure 8 also reports the conductivities σ_{YSZ} and σ_{CeO_2} used to calculate σ^* and the conductivity of single-crystal 9.5YSZ from ref 18. The conductivity of sample D calculated using the diffusion coefficient measured by SIMS is also reported for comparison in the same figure.

The conductivity of sample E is very similar to σ^* and shows the same activation energy. Analogous results were obtained for all of the tested heterostructures.

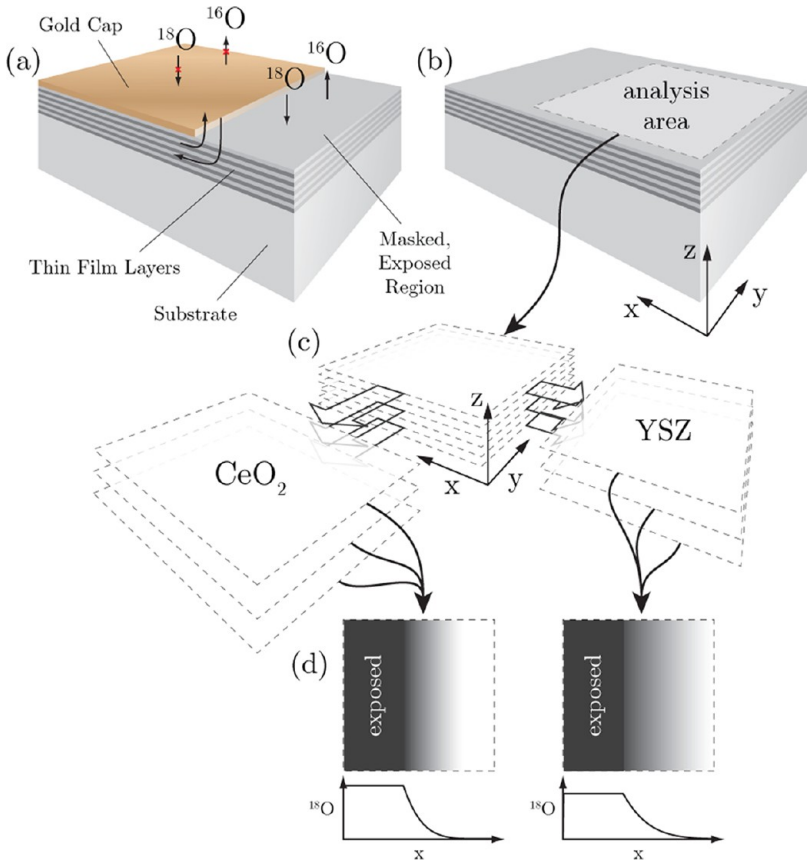

Figure 9. Sample is gold-coated with a region masked off, as shown schematically in (a), the sample is exposed to an ^{18}O-enriched atmosphere allowing $^{16}O-^{18}O$ exchange solely at the trench edge. The gold capping layer is then removed, allowing SIMS analysis (b), resulting in a three-dimensional data set (c), which can be separated into layer types. The resulting series of ion images on the $x-y$ plane can be integrated along the z axis (d) allowing relatively low noise line scans to be extracted for each layer type.

In other words, each heterostructure showed the same conductivity and activation energy of a fully relaxed YSZ-CeO_2 bilayer. This finding implies that the 8YSZ thin layers in all of the heterostructures fabricated for this work showed the same conducting properties as YSZ bulk, independently on the number of interfaces (from 4 to 60) and down to a minimum single-layer thickness as small as 5 nm.

Conductivity measurements were also performed for every sample at constant temperature (550 and 650 °C) as a function of the oxygen partial pressure between 1 and 10^{-4} atm. Throughout the investigated range of oxygen partial pressure, an almost constant value of conductivity was measured for each sample at each temperature. This finding combined with the tracer diffusivity measurements identifies the oxygen ions as the main charge carriers for the fabricated heterostructures under the experimental condition selected for the conductivity measurements reported in this work.

Finally, it is worth noticing that, since the increasing number of interfaces did not affect the mobility, the nature, and the concentration of the charge carriers, these measurements suggest that also a potential interfacial space charge effect plays a negligible role in affecting the conducting properties.

CONCLUSIONS

The unambiguous identification of the potential interfacial strain effects on the ionic conductivity requires the fabrication of appropriately designed samples in which every possible spurious contribution to the total conductivity is suppressed. This work reports the fabrication and electrical characterization of 8YSZ-CeO_2 heterostructures in which the only active contributions were those parallel to the bulk and the interface regions. In detail, the charge transport through the fabricated heterostructures could not be influenced by the deposition substrate, the grain boundary conduction pathways, or the misfit dislocation conducting planes.

Depth profiles performed by ToF-SIMS revealed excellent quality films showing high uniformity over a large area with very little cation interdiffusion and no significant levels of contamination. Oxygen isotope tracer measurements were performed and allowed determination of diffusion coefficients in each layer type. The 8YSZ layers were seen to be those with the

fastest oxygen diffusion, and the ionic contribution gave a value in good agreement with bulk YSZ and those determined from EIS measurements. This confirms that the dominant charge carrier in the samples is oxygen. These ToF-SIMS measurements have demonstrated a novel technique for measuring both oxygen diffusion and chemical profiles in ionically conducting thin film and multilayer samples such as these.

Keeping constant the total thickness of the conductor at about 300 nm, the number of heterointerfaces was increased from 4 to 60 by reducing the thickness of each individual layer down to a minimum thickness of about 10 unit cells. The analysis of the EIS results showed the same values of conductivity and activation energy for all of the samples. Moreover, such values are in very good agreement with the theoretical conductivity expected for a fully relaxed and highly textured bilayer of the two materials, implying that the 8YSZ layers in the heterostructures always showed bulk conductivity without any significant contribution from the interfaces.

Even though the interfacial roughness made questionable any attempt to quantify the strength of the residual strain field, GPA and XRD analysis showed several regions of the 8YSZ interfaces subjected to a lattice distortion that matched the theoretical lattice misfit of about 5%. This finding implies that the interfaces are non-uniformly but significantly strained. However, for the described samples from the interface regions no detectable contribution to the total conductivity occurred over the threshold of the 8YSZ bulk conductivity, even in the case of layers as thin as about 10 unit cells.

METHODS

Biaxially textured, (001) epitaxially oriented heterostructures made of 8 mol % Y_3O_2-stabilized ZrO_2 (YSZ) and CeO_2 were prepared by pulsed laser deposition (PLD). Commercially available (001)-oriented single-crystal MgO wafers were selected as deposition substrates. A buffer layer of $SrTiO_3$ (STO), about 10 nm thick, was deposited *in situ* onto the substrate surface, providing the required crystalline matching for the growth of the heterostructures.

The custom-made PLD system used (AOV Ltd., Tokyo) consisted of a vacuum chamber with a base pressure of about 10^{-6} Pa equipped with a boron carbide resistive heater, a multitarget carrousel, and a load-lock chamber. The MgO wafer pretreatment consisted of ultrasonically cleaning in acetone and isopropyl alcohol, drying with N_2, and *in situ* annealing at 800 °C for at least 30 min at a relatively high O_2 partial pressure (about 50 Pa). The substrate temperature during the deposition process was set at about 700 °C. The thermal contact between the sample holder and the deposition substrate was provided by Au paste. A gas inlet line allowed setting a high purity oxygen partial pressure of about 5 Pa during the deposition. The target to substrate distance was set at 75 mm. A KrF excimer laser (Coherent Lambda Physik GmbH) with a wavelength of 248 nm and a pulse width of 25 ns was focused on the target material in a spot area of about 5 mm^2 with an energy of about 160 mJ (measured at the target surface) and a repetition rate between 2 and 5 Hz. During the ablation process, each target was rotating and oscillating, allowing a uniform ablation of the target surface, while a stainless steel shield avoided cross-contamination of the targets. The pulsed laser was used to ablate 8YSZ, CeO_2, and STO sintered pellets prepared in our laboratory. A programmable control unit allowed programming multistep deposition processes selecting for each subsequent step the target material, the target oscillation amplitude and velocity, the number of laser shots and the laser frequency for each target.

XRD (PANalytical X'pert Pro MPD) analysis was used for the calibration of the deposition rate by X-ray reflectivity and to investigate the crystalline structure of the films. The $2\theta/\theta$ scans were measured to check the epitaxial orientation of the depositions. Reciprocal space maps toward the (204), (103), and (113) asymmetric reflections of MgO, STO, and CeO_2, respectively, were acquired to investigate the in-plane texture of the heterostructures.

High-resolution transmission electron microscopy (HR-TEM) was carried out using a Tecnai F20ST electron microscope equipped with a high-angle annular dark-field detector and operated at 200 kV. Samples for HR-TEM analysis were prepared by standard techniques, including mechanical polishing followed by ion milling using Fischione 1010 ion mill.

To allow oxygen tracer diffusion measurements by secondary ion mass spectroscopy (SIMS), samples were first annealed at 800 °C in 200 mbar of research grade oxygen for >48 h to allow full oxidation of the films and provide comparability with the measurements performed by electrochemical impedance spectroscopy (EIS), and then gold-coated (~180 nm) using an Emitech K575x turbo sputter coater (Emitech LTD), blocking oxygen exchange at the film surface, while a mask was used to leave a region exposed. The masked region (Figure 9a) allowed exposure to the ^{18}O-enriched atmosphere, and thus the subsequent diffusion occurred under the gold capping layer, in a direction parallel to the sample interfaces and in the same direction as the electrical characterization. After the anneal and oxygen exchange, the surface gold layer was removed by a combination of agitation in acetone and light abrasion of the surface with a cotton swab prior to SIMS analysis (indicated in Figure 9b). The coated sample was first annealed at the desired exchange temperature for time t_{anneal} in 200 mbar of oxygen with natural isotopic abundance (~0.2%) and then in an ^{18}O-enriched atmosphere at the same pressure and temperature for time $t_{exchange}$ where $t_{anneal} \gg t_{exchange}$ ($t_{exchange}$ = 3280 s, T = 487 °C, pO_2 = 200 mbar).

Compositional and isotopic depth profiling was performed by time-of-flight secondary ion mass spectroscopy (ToF-SIMS) on samples A–E on a TOF.SIMS[5] (ION-TOF GmbH, Münster, Germany). Compositional depth profile analyses were performed with a 500 × 500 μm raster of the Cs^+ sputter beam at 2 keV and a rastered 25 keV Bi^+ beam over an analysis region of 100 × 100 μm (128 × 128 pixels). Charge compensation was required due to the insulating properties of the samples and achieved with the use of an electron flood gun. Positive ions were collected for compositional profiles as this showed greater sensitivity to the matrix species of interest. Negative secondary ions were used to obtain oxygen isotopic profiles. Sputtering through the entire film depth resulted in approximately 2000 individual analysis planes each consisting of 128 × 128 pixels. Each pixel contains a mass spectrum, thus post-analysis, by selecting an appropriate mass and region of pixels, one can produce a depth profile. Depth calibration of SIMS depth profiles was performed by measuring ablated crater depths postanalysis using a Zygo NewView 200 white-light microscope-based interferometer.

One advantage of the utilization of ToF-SIMS in this work is the ability to selectively reconstruct data post-analysis from a data set with three dimensions and a mass spectrum for each pixel. A measurement with both a high lateral (256 × 256 pixels, 200 μm^2) and subnanometer depth resolution was performed in a region surrounding the edge of the gold. This produced a three-dimensional data set using negative secondary ions (represented in Figure 9c), which could later be reconstructed in various regions of interest, such as depth profiles on the z axis in certain $x-y$ regions or ion images of the $x-y$ plane of selected z depths.

For the electrical measurements, two parallel strip-shaped Ti−Pt electrodes were deposited on the film surface at a distance of 1 mm, over an area of about (5×2) mm^2, and wired to the read-out electronics using Pt paste and wires. Electron beam deposition was used for the thermal evaporation of Ti and Pt. Then, 10 nm of Ti and 100 nm of Pt films were deposited *in situ* at a base pressure of about 5×10^{-5} Pa to vacuum, using an accelerating voltage of 20 kV and an emission current of about 80 and 250 mA, respectively, achieving a deposition rate between 1 and 2 Å/s. The electrodes were deposited at room temperature and patterned by stencil mask.

Electrochemical impedance spectroscopy (EIS) measurements were performed between 1 MHz and 100 mHz in air, varying the temperature between 400 and 700 °C, using a multichannel potentiostat VMP3 (Bio-Logic). The charge carrier nature and relative influence on the charge transport through the films were studied by acquiring EIS measurements varying the oxygen partial pressure of the surrounding gaseous environment between 1 and 10^{-4} atm, using O_2-N_2 and air$-N_2$ gas mixtures, and monitoring the oxygen partial pressure of the outlet gas with a zirconia oxygen sensor.

Conflict of Interest: The authors declare no competing financial interest.

Acknowledgment. This work was partly supported by the World Premier International Research Centre Initiative of MEXT, Japan.

Supporting Information Available: In section 1, more details are given concerning the HR-TEM analysis of the fabricated heterostructures. Section 2 reports the results of the RSM measurements of an additional CeO_2-YSZ superlattice. This analysis supports the conclusions obtained by GPA concerning the presence of a nonuniform but significant strain along the layers. Section 3 shows the analysis of the compositional depth profile using SIMS of the heterostructures fabricated for this work. This material is available free of charge *via* the Internet at http://pubs.acs.org.

REFERENCES AND NOTES

1. Kilner, J. A. Ionic Conductors: Feel the Strain. *Nat. Mater.* **2008**, *7*, 838–839.
2. Guo, X.; Maier, J. Ionically Conducting Two-Dimensional Heterostructures. *Adv. Mater.* **2009**, *21*, 2619–2631.
3. Fabbri, E.; Pergolesi, D.; Traversa, E. Ionic Conductivity in Oxide Heterostructures: The Role of Interfaces. *Sci. Technol. Adv. Mater.* **2010**, *11*, 054503.
4. Azad, S.; Marina, O. A.; Wang, C. M.; Saraf, L.; Shutthanandan, V.; McCready, D. E.; El-Azab, A.; Jaffe, J. E.; Engelhard, M. H.; Peden, C. H. F.; *et al.* Nanoscale Effects on Ion Conductance of Layer-by-Layer Structures of Gadolinia-Doped Ceria and Zirconia. *Appl. Phys. Lett.* **2005**, *86*, 131906.
5. Kosacki, I.; Rouleau, C. M.; Becher, P. F.; Bentley, J.; Lowndes, D. H. Nanoscale Effects on the Ionic Conductivity in Highly Textured YSZ Thin Films. *Solid State Ionics* **2005**, *176*, 1319–1326.
6. Garcia-Barriocanal, J.; Rivera-Calzada, A.; Varela, M.; Sefrioui, Z.; Iborra, E.; Leon, C.; Pennycook, S. J.; Santamaria, J. Colossal Ionic Conductivity at Interfaces of Epitaxial ZrO_2:Y_2O_3/$SrTiO_3$ Heterostructures. *Science* **2008**, *321*, 676–680.
7. Schichtel, N.; Korte, C.; Hesse, D.; Janek, J. Elastic Strain at Interfaces and Its Influence on Ionic Conductivity in Nanoscaled Solid Electrolyte Thin Films—Theoretical Considerations and Experimental Studies. *Phys. Chem. Chem. Phys.* **2009**, *11*, 3043–3048.
8. Sanna, S.; Esposito, V.; Tebano, A.; Licoccia, S.; Traversa, E.; Balestrino, G. Enhancement of Ionic Conductivity in Sm-Doped Ceria/Yttria-Stabilized Zirconia Heteroepitaxial Structures. *Small* **2010**, *6*, 1863–1867.
9. Sillassen, M.; Eklund, P.; Pryds, N.; Johnson, E.; Helmersson, U.; Bøttiger, J. Low-Temperature Superionic Conductivity in Strained Yttria-Stabilized Zirconia. *Adv. Funct. Mater.* **2010**, *20*, 2071–2076.
10. Korte, C.; Peters, A.; Janek, J.; Hesse, D.; Zakharov, N. Ionic Conductivity and Activation Energy for Oxygen Ion Transport in Superlattices—The Semicoherent Multilayer System YSZ (ZrO_2 + 9.5 mol% Y_2O_3)/Y_2O_3. *Phys. Chem. Chem. Phys.* **2008**, *10*, 4623–4635.
11. Guo, X. Comment on "Colossal Ionic Conductivity at Interfaces of Epitaxial ZrO_2:Y_2O_3/$SrTiO_3$ Heterostructures". *Science* **2009**, *324*, 465a.
12. Peters, A.; Korte, C.; Hesse, D.; Zakharov, N.; Janek, J. Ionic Conductivity and Activation Energy for Oxygen Ion Transport in Superlattices—The Multilayer System CSZ (ZrO_2 + CaO)/Al_2O_3. *Solid State Ionics* **2007**, *178*, 67–76.
13. Schichtel, N.; Korte, C.; Hesse, D.; Zakharov, N.; Butz, B.; Gerthsen, D.; Janek, J. On The Influence of Strain on Ion Transport: Microstructure and Ionic Conductivity of Nanoscale YSZ | [Sc_2O_3 Multilayers]. *Phys. Chem. Chem. Phys.* **2010**, *12*, 14569–14608.
14. Kuwata, N.; Sata, N.; Tsurui, T.; Yugami, H. Proton Transport and Microstructure Properties in Superlattice Thin Films Fabricated by Pulsed Laser Deposition. *Jpn. J. Appl. Phys.* **2005**, *44*, 8613–8618.
15. Kuwata, N.; Sata, N.; Saito, S.; Tsurui, T.; Yugami, H. Structural and Electrical Properties of $SrZr_{0.95}Y_{0.05}O_3$/$SrTiO_3$ Superlattices. *Solid State Ionics* **2006**, *177*, 2347–2351.
16. Korte, C.; Schichtel, N.; Hesse, D.; Janek, J. Influence of Interface Structure on Mass Transport in Phase Boundaries between Different Ionic Materials. *Monatsh. Chem.* **2009**, *140*, 1069–1080.
17. Heiroth, S.; Lippert, Th.; Wokaun, A.; Döbeli, M. Microstructure and Electrical Conductivity of YSZ Thin Films Prepared by Pulsed Laser Deposition. *Appl. Phys. A: Mater. Sci. Process.* **2008**, *93*, 639–643.
18. Göbel, M. C.; Gregori, G.; Guo, X.; Maier, J. Boundary Effects on the Electrical Conductivity of Pure and Doped Cerium Oxide Thin Films. *Phys. Chem. Chem. Phys.* **2010**, *12*, 14351–14361.
19. Manning, P .S.; Sirman, J. D.; De Souza, R. A.; Kilner, J. A. The Kinetics of Oxygen Transport in 9.5 mol % Single Crystal Yttria Stabilised Zirconia. *Solid State Ionics* **1997**, *100*, 1–10.
20. Sanna, S.; Esposito, V.; Pergolesi, D.; Orsini, A.; Tebano, A.; Licoccia, S.; Balestrino, G.; Traversa, E. Fabrication and Electrochemical Properties of Epitaxial Samarium-Doped Ceria Films on $SrTiO_3$-Buffered MgO Substrates. *Adv. Funct. Mater.* **2009**, *19*, 1713–1719.
21. Chen, C. H.; Kiguchi, T.; Saiki, A.; Wakiya, N.; Shinozaki, K.; Mizutani, N. Characterization of Defect Type and Dislocation Density in Double Oxide Heteroepitaxial CeO_2/YSZ/Si(001) Films. *Appl. Phys. A: Mater. Sci. Process.* **2003**, *76*, 969–973.
22. Sayle, T. X. T.; Parker, S. C.; Sayle, D. C. Ionic Conductivity in Nano-scale CeO_2/YSZ Heterolayers. *J. Mater. Chem.* **2006**, *16*, 1067–1081.
23. Hytch, M. J. Geometric Phase Analysis of High Resolution Electron Microscope Images. *Scanning Microsc.* **1997**, *11*, 53–66.
24. Gutakovskii, A. K.; Chuvilin, A. L.; Song, S. A. Izvestiya Rossiiskoi Akademii Nauk. *Ser. Fiz.* **2007**, *71*, 1464–1470.
25. Wang, C. M.; Thevuthasan, S.; Peden, C. H. F. Interface Structure of an Epitaxial Cubic Ceria Film on Cubic Zirconia. *J. Am. Ceram. Soc.* **2003**, *86*, 363–365.
26. Pergolesi, D.; Tebano, A.; Fabbri, E.; Balestrino, G.; Licoccia, S.; Traversa, E. Pulsed Lased Deposition of Superlattices Based on Ceria and Zirconia. *ECS Transactions* **2011**, *35*, 1125–1130.
27. Crank, J. *The Mathematics of Diffusion*, 2nd ed.; Oxford University Press: Oxford, UK, 1975.
28. *Matlab R2011a*, The MathWorks Inc, 2011.
29. Perkins, J. M.; Fearn, S.; Cook, S. N.; Srinivasan, R.; Rouleau, C. M.; Christen, H. M.; West, G. D.; Morris, R. J. H.; Fraser, H. L.; Skinner, S. J.; *et al.* Anomalous Oxidation States in Multilayers for Fuel Cell Applications. *Adv. Funct. Mater.* **2010**, *20*, 2664–2674.
30. Barsoum, M. *Fundamentals of Ceramics*; Taylor & Francis: London, 2003.